

Two-phase resonant patterns in forced oscillatory systems: boundaries, mechanisms and forms

Arik Yochelis^{a,*}, Christian Elphick^b, Aric Hagberg^c, Ehud Meron^{a,d}

^a *Department of Physics, Ben-Gurion University, Beer Sheva 84105, Israel*

^b *Centro de Física No Lineal y Sistemas Complejos de Santiago, Casilla 17122, Santiago, Chile*

^c *Mathematical Modeling and Analysis, Theoretical Division, Los Alamos National Laboratory, Los Alamos, NM 87545, USA*

^d *Department of Solar Energy and Environmental Physics, BIDR, Ben Gurion University, Sede Boker Campus 84990, Israel*

Abstract

We use the forced complex Ginzburg–Landau (CGL) equation to study resonance in oscillatory systems periodically forced at approximately twice the natural oscillation frequency. The CGL equation has both resonant spatially uniform solutions and resonant two-phase standing-wave pattern solutions such as stripes or labyrinths. The spatially uniform solutions form a tongue-shaped region in the parameter plane of the forcing amplitude and frequency. But the parameter range of resonant standing-wave patterns does not coincide with the tongue of spatially uniform oscillations. On one side of the tongue the boundary of resonant patterns is inside the tongue and is formed by the nonequilibrium Ising Bloch bifurcation and the instability to traveling waves. On the other side of the tongue the resonant patterns extend outside the tongue forming a parameter region in which standing-wave patterns are resonant but uniform oscillations are not. The standing-wave patterns in that region appear similar to those inside the tongue but the mechanism of their formation is different. The formation mechanism is studied using a weakly nonlinear analysis near a Hopf–Turing bifurcation. The analysis also gives the existence and stability regions of the standing-wave patterns outside the resonant tongue. The analysis is supported by numerical solutions of the forced complex Ginzburg–Landau equation.

© 2004 Elsevier B.V. All rights reserved.

Keywords: Resonant pattern; Forced oscillatory system; Ginzburg–Landau equation

1. Introduction

Resonance phenomena in forced oscillatory systems have mostly been studied in the context of a single oscillator such as the pendulum [1–3]. The resonant behavior is manifested by the ability of the system to adjust its natural oscillation frequency to a rational fraction of the forcing frequency. Thus, the system may respond, or lock, in ratios

* Corresponding author.

E-mail addresses: yochelis@bgumail.bgu.ac.il (A. Yochelis); lelphick@vtr.net (C. Elphick); hagberg@lanl.gov (A. Hagberg); ehud@bgumail.bgu.ac.il (E. Meron)

$1/n$ ($n = 1, 2, 3, \dots$) of the forcing frequency and at additional fractions determined by the Farey hierarchy [4]. The natural frequency range, where the system locks to the forcing frequency, increases with the forcing amplitude and forms a tongue-shaped region (Arnol'd tongues) in the amplitude–frequency plane. The parameter region pertaining to oscillations at $1/n$ the forcing frequency is occasionally referred to as the n : 1 resonance tongue.

More recently resonance phenomena have been studied in spatially extended systems using uniform time periodic forcing [5–21]. These systems demonstrate another property of resonance phenomena; although any spatial point in the system oscillates at the same fraction $1/n$ of the forcing frequency, the phase of oscillation may assume one of n different values and may vary from one spatial domain to another [8,22]. In the 2:1 resonance, there are two stable phases of oscillations (differing from one another by π) and fronts that shift the oscillation phase by π may appear. In the 4:1 resonance, there are four stable phases and two types of fronts may appear; fronts can shift the oscillation phases by either π or $\pi/2$. Along with these fronts spatial patterns, such as spiral waves and standing-wave labyrinths, may appear [10,12,20].

In this paper, we study to the 2:1 resonance case and the conditions for resonant behavior in spatially extended systems as compared with those of a single oscillator. The study is based on a variant of the complex Ginzburg–Landau (CGL) equation which describes the dynamics of the oscillation amplitude near the Hopf bifurcation. Among our findings are non-resonant patterns in a range of resonant uniform oscillations and resonant patterns in a range where uniform oscillations are not resonant. The results derived in this paper extend the analytical and numerical results presented in Ref. [20].

The paper is organized as follows. In Section 2, we derive the boundaries of the 2:1 resonance tongue for uniform oscillations. This is the domain where the system is bistable and front solutions may exist. In Section 3, we study two front instabilities and the patterns that arise from them. The results are used to determine the range where resonant patterns appear inside the 2:1 resonant tongue of uniform oscillations. In Section 4, we determine the conditions for the prevalence of resonant standing waves *outside* the resonance tongue and show that the formation mechanism differs from that of standing waves inside the tongue. We conclude with a summary and a discussion of the results in Section 5.

2. The 2:1 resonance tongue

Consider an extended system undergoing a Hopf bifurcation to uniform oscillations at a frequency Ω . The system is now uniformly forced at a frequency $\omega_f \approx 2\Omega$. Near the Hopf bifurcation a typical dynamical variable of the system can be written as

$$u = u_0 + [A e^{i\omega t} + \text{c.c.}] + \dots, \quad (1)$$

where u_0 is the value of u when the system is at the rest state undergoing the Hopf bifurcation, A is a complex amplitude, $\omega := \omega_f/2$, c.c. stands for the complex conjugate, and the ellipses denote higher order terms. The amplitude of oscillation A is slowly varying in space and time and for weak forcing is described by the forced CGL equation [23–26]

$$\partial_t A = (\mu + i\nu)A + (1 + i\alpha)\nabla^2 A - (1 + i\beta)|A|^2 A + \gamma A^*. \quad (2)$$

In this equation, μ represents the distance from the Hopf bifurcation, $\nu = \Omega - \omega_f/2$ the detuning, α represents dispersion, β represents nonlinear frequency correction, γ the forcing amplitude, and ∇^2 is the two-dimensional Laplacian operator. The term A^* is the complex conjugate of A and describes the effect of the weak periodic forcing [23]. Throughout this paper, we will mostly be concerned with Eq. (2) for the amplitude of oscillations. The oscillating system in Eq. (1) will be referred to as the “original system.”

To find the resonance boundary of uniform oscillations, we write $A = \mathcal{R} \exp(i\phi)$ and consider uniform solutions of Eq. (2). The amplitude \mathcal{R} and the phase ϕ obey the equations:

$$\dot{\mathcal{R}} = \mu\mathcal{R} - \mathcal{R}^3 + \gamma\mathcal{R} \cos 2\phi, \tag{3a}$$

$$\dot{\phi} = \nu\mathcal{R} - \beta\mathcal{R}^3 - \gamma\mathcal{R} \sin 2\phi. \tag{3b}$$

In 2:1 resonance the system oscillates at exactly half of the forcing frequency. According to Eq. (1), this condition is satisfied by stationary solutions of \mathcal{R} and ϕ . These solutions appear in a pair of saddle node bifurcations at $\gamma = \gamma_b$ [7], where

$$\gamma_b = \frac{|v - \mu\beta|}{\sqrt{1 + \beta^2}}, \tag{4}$$

as Fig. 1(a) shows. The form of the resonance boundary changes to

$$\gamma_b = \frac{1}{2} \sqrt{\mu^2 + (\mu\beta - 2\nu)^2}$$

for $\nu < \mu(\beta^2 - 1)/(2\beta)$ (assuming $\beta > 0$ which is used here). For further details see Ref. [27]. The two stable solutions are given by

$$\phi_- = \frac{1}{2} \arcsin \frac{\nu - \beta(\tilde{\mu} + \tilde{\gamma})}{\gamma}, \tag{5a}$$

$$\phi_+ = \phi_- + \pi, \tag{5b}$$

where $\tilde{\mu} = (\mu + \nu\beta)/(1 + \beta^2)$, $\tilde{\gamma} = \sqrt{\gamma^2/(1 + \beta^2) - \tilde{\nu}^2}$, and $\tilde{\nu} = (\nu - \mu\beta)/(1 + \beta^2)$.

We refer to the solutions ϕ_- and ϕ_+ as “phase locked” solutions or “phase states.” The existence range of these solutions, $\gamma \geq \gamma_b$, forms a V-shape region, hereafter the “2:1 resonance tongue.” The 2:1 resonance tongue for $\beta = 0$

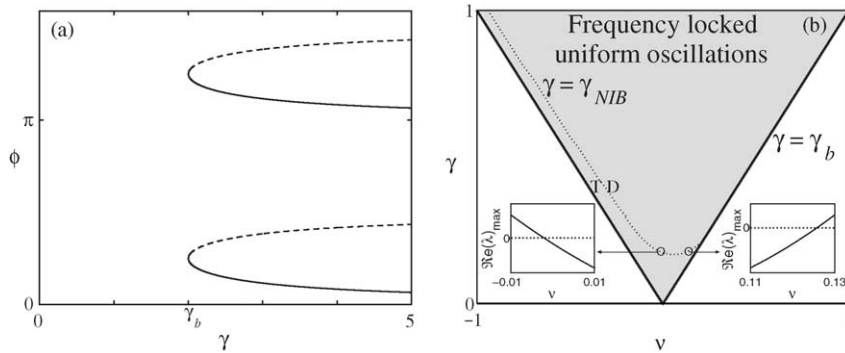


Fig. 1. (a) A pair of saddle-node bifurcation diagrams showing the appearance of the four stationary phase solutions of Eq. (5a) as the forcing amplitude γ is increased past γ_b for a fixed detuning value ν . The solid (dashed) curves represent stable (unstable) solutions. (b) The resonance tongue in the ν - γ plane (shaded region) inside which the original system responds at exactly half the forcing frequency. Also shown is the NIB bifurcation threshold (dotted curve) inside the resonance tongue, obtained by numerically solving the one-dimensional eigenvalue problem of Eq. (8) for a front solution of Eq. (2). The NIB bifurcation threshold corresponds to a zero value of the largest real part of the eigenvalue λ (not including the zero eigenvalue associated with translation) as the two insets show, $\gamma = 0.18$. Above the NIB bifurcation threshold fronts bi-asymptotic to the two stable phase states, ϕ_- and ϕ_+ , are stationary. The points “D” ($\gamma = 0.4$, $\nu = -0.3$) and “T” ($\gamma = 0.4$, $\nu = -0.38$) represent forcing and detuning values where the Ising fronts are stable and unstable to NIB bifurcation, respectively. Parameters: $\mu = 0.5$, $\beta = 0$, $\alpha = 0.5$.

is shown in Fig. 1(b). For $\beta \neq 0$ the tongue gets wider and is shifted to the right ($\beta > 0$) or to the left ($\beta < 0$). Outside the resonance tongue uniform solutions describe unlocked oscillations.

For the analysis that follows we rewrite Eq. (2) in terms of the real and imaginary parts of the amplitude, $U := \text{Re } A$ and $V := \text{Im } A$:

$$\begin{pmatrix} \partial_t U \\ \partial_t V \end{pmatrix} = (\mathcal{L} - \mathcal{N}) \begin{pmatrix} U \\ V \end{pmatrix}, \quad (6)$$

where \mathcal{L} is the linear operator

$$\mathcal{L} = \begin{bmatrix} (\mu + \gamma) + \nabla^2 & -\nu - \alpha \nabla^2 \\ \nu + \alpha \nabla^2 & (\mu - \gamma) + \nabla^2 \end{bmatrix},$$

and \mathcal{N} includes the nonlinear terms

$$\mathcal{N} = (U^2 + V^2) \begin{bmatrix} 1 & -\beta \\ \beta & 1 \end{bmatrix}.$$

3. Spatial patterns inside the 2:1 resonance tongue

Inside the 2:1 resonance tongue the system is bistable and front solutions, bi-asymptotic to the two stable phase states, exist. Patterns in bistable systems are strongly affected by two types of front instabilities [28,29]. The first is the nonequilibrium Ising Bloch (NIB) bifurcation in which a stationary “Ising” front solution loses stability to a pair of counter-propagating “Bloch” front solutions. This instability designates a transition from stationary patterns to traveling waves. The second front instability is a transverse instability (occasionally also referred to as modulational or morphological instability) where wiggles along the front line grow in time. A transverse front instability of an Ising front often leads to stationary labyrinthine patterns. In the context of forced oscillations the NIB bifurcation has been studied in Refs. [7,30–33] and the transverse instability in Ref. [17]. In the following we extend these earlier works and use the results to delineate the range within the 2:1 resonance tongue where resonant patterns reside.

Finite wavenumber instabilities of the uniform phase states may also lead to pattern formation inside the 2:1 resonance tongue. A linear stability analysis of the phase states indeed reveals such an instability but in a very narrow range near the 2:1 resonance boundary. The instability leads to large amplitude stationary patterns representing resonant oscillations of the original system. For further details the reader is referred to Ref. [27]. In the following analyzes performed inside the tongue we assume a parameter range for which the phase states are stable to nonuniform perturbations.

3.1. The nonequilibrium Ising Bloch (NIB) bifurcation

In the case, $\alpha = \beta = 0$, the NIB bifurcation occurs at $\gamma_{\text{NIB}} = \sqrt{\nu^2 + (\mu/3)^2}$ [32,33]. To evaluate the NIB bifurcation across the resonance tongue for non-zero α or β values we use a numerical eigenvalue analysis of the Ising front solution $\mathbf{I}(x)$. Inserting the form

$$\begin{bmatrix} U(x, t) \\ V(x, t) \end{bmatrix} = \mathbf{I}(x) + \mathbf{e}(x) e^{\lambda t}, \quad (7)$$

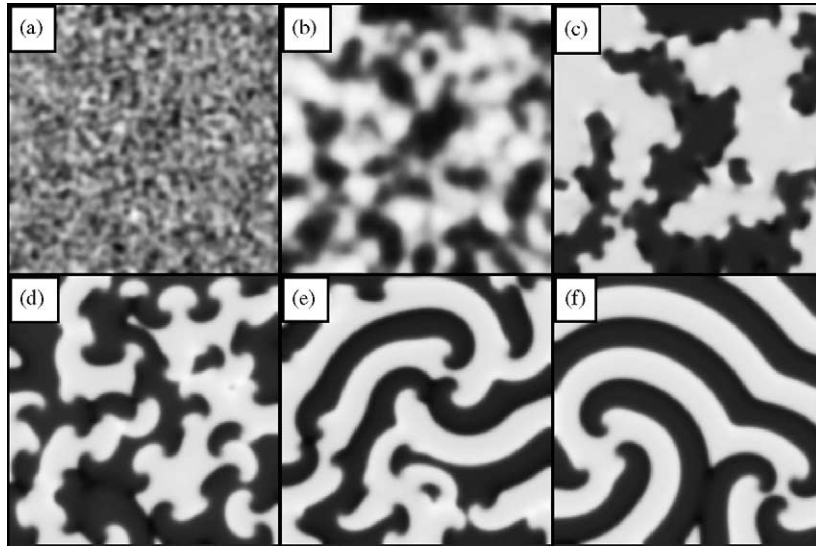


Fig. 2. A numerical solution of Eq. (6) in the range $\gamma_b < \gamma < \gamma_{\text{NIB}}$ [point “T” in Fig. 1(b)], showing the development of spiral waves from small random perturbations around the unstable rest state, $U = V = 0$. The pattern corresponds to unlocked spiral waves in the original system since $\omega \neq \omega_f/2$. The frames (a)–(f) show a grey-scale map of the U field at successive time steps: $t = 1.5, 8.5, 19, 90, 2000, 6000$. In all of the grey-scale figures darker hues denote higher U values. Neumann boundary conditions were used on a domain $x = [0, 80], y = [0, 80]$. Parameters are as in Fig. 1(b), $\nu = -0.38, \gamma = 0.4$.

in Eq. (6) and linearizing around $\mathbf{I}(x)$ we obtain

$$[J(U, V) - \lambda \mathcal{I}] \mathbf{e} = 0, \quad (8)$$

where $J(U, V)$ is the Jacobian of Eq. (6) at $\mathbf{I}(x)$, λ the eigenvalue, $\mathbf{e}(x)$ the eigenvector, \mathcal{I} the identity matrix, and the form of $\mathbf{I}(x)$ is obtained by numerical integration of Eq. (6). Solving (8) for λ we identify the NIB bifurcation threshold as the value $\gamma = \gamma_{\text{NIB}}(\nu)$ at which the largest real part of the eigenvalue λ is zero (excluding the zero eigenvalue associated with the translation mode). The NIB bifurcation threshold in the ν – γ plane and for $\alpha > 0$ is shown in Fig. 1(b).

For $\gamma_b < \gamma < \gamma_{\text{NIB}}$ spiral waves prevail. Fig. 2 shows numerical solutions of Eq. (6) in this range displaying the development of rotating spiral waves starting from random perturbations of the unstable rest state $A = 0$. Since the amplitude A oscillates at the spiral frequency ω_s , the original system [see Eq. (1)] oscillates at a frequency $\omega_f/2 + \omega_s$ rather than $\omega_f/2$ and therefore is out of resonance.

As the NIB bifurcation is traversed stationary Ising fronts appear. The same random perturbations of the unstable rest state (as in Fig. 2) now lead to coarsening and to the formation of larger domain patterns as Fig. 3 shows. Since the domain boundaries approach stationary planar Ising fronts the patterns represent resonant oscillations. We now turn over to the high frequency side of the 2:1 resonance tongue.

3.2. Transverse instability of the Ising front

As ν is increased, and the high frequency boundary of the 2:1 resonance tongue is approached, a transverse front instability is encountered [17,20]. The onset of this instability, $\gamma = \gamma_{\text{T}}$ ($\gamma_{\text{T}} > \gamma_{\text{NIB}}$), is shown by the dashed line in Fig. 4. The significance of the transverse front instability is demonstrated in Fig. 5; a planar Ising front evolves to a labyrinthine pattern through fingering and tip splitting. The asymptotic pattern is stationary and therefore represents resonant oscillations.

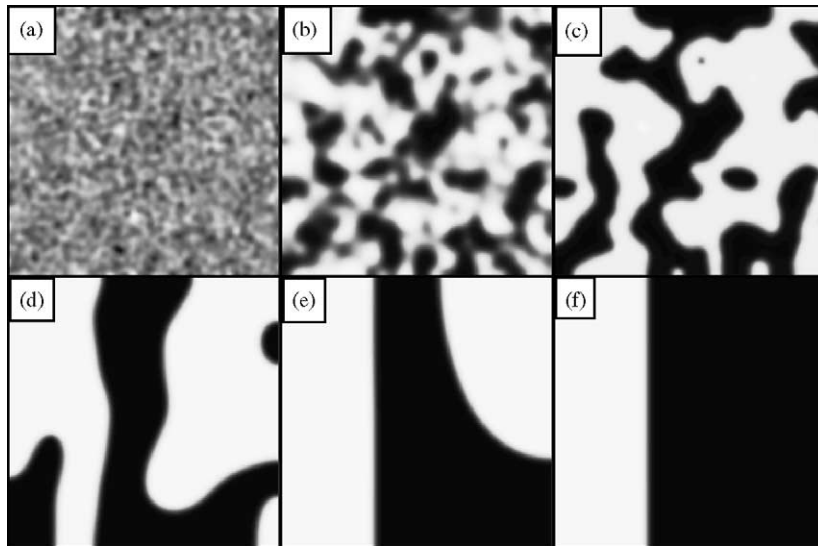


Fig. 3. A numerical solution of Eq. (6) in the range $\gamma_{\text{NIB}} < \gamma$ [point “D” in Fig. 1(b)] showing the coarsening of small domains into larger ones separated by a planar Ising front. The asymptotic state is resonant since the Ising front is stationary and any point in the original system it oscillates at exactly $\omega = \omega_f/2$. The frames (a)–(f) show the U field at successive time steps: $t = 1.5, 8.5, 19, 90, 350, 850$. Neumann boundary conditions were used on a domain $x = [0, 80], y = [0, 80]$. Parameters are as in Fig. 1(b), $\nu = -0.3, \gamma = 0.4$.

We evaluated the transverse instability boundary by deriving a linear evolution equation for transverse front modulations as we now describe. Eq. (6), for $\alpha = \beta = 0$ (but arbitrary ν), has the exact Ising front solution

$$U_0 = I(x) \cos \phi, \tag{9a}$$

$$V_0 = I(x) \sin \phi, \tag{9b}$$

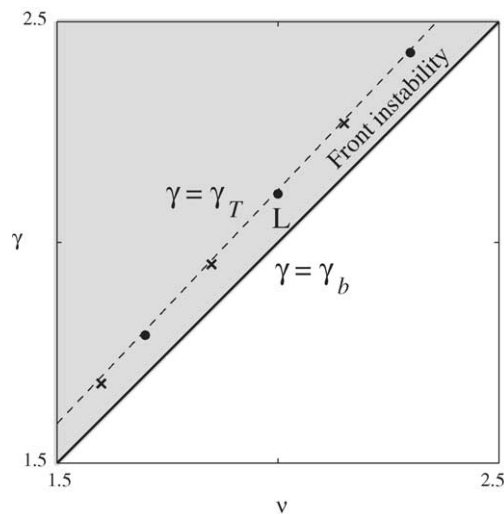


Fig. 4. The transverse instability line, $\gamma = \gamma_T$, for an Ising front inside the 2:1 resonance tongue. The dashed line denotes the approximate analytical result of γ_T given by Eq. (24). The crosses (\times) depict the condition $D = 0$ where D is calculated semi-analytically using Eq. (20), while the solid circles (\bullet) represent results of a numerical two-dimensional eigenvalue analysis of the Ising front. Parameters: $\mu = 0.5, \alpha = 0.35, \beta = 0$.

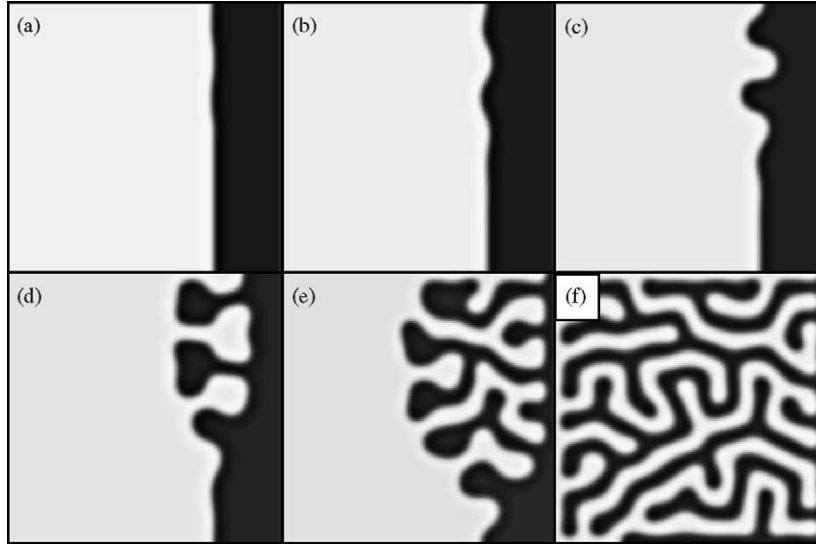


Fig. 5. A numerical solution of Eq. (6) in the range $\gamma_b < \gamma < \gamma_T$ (point “L” in Fig. 4), showing the development of a stationary labyrinthine pattern from a transverse instability of a planar Ising front. The pattern corresponds to resonant labyrinthine standing waves in the original system. The frames (a–f) show the U field at successive time steps: $t = 0, 150, 250, 400, 600, 1400$. Neumann boundary conditions were used on a domain $x = [0, 77], y = [0, 77]$. Parameters: $\nu = 2.0, \gamma = 2.05$, and other parameters as in Fig. 4.

where $\phi = 1/2 \arccos(\hat{\gamma}/\gamma)$, $\hat{\gamma} = \sqrt{\gamma^2 - \nu^2}$, and $I(x)$ is given by

$$I(x) = \pm \sqrt{\mu + \hat{\gamma}} \tanh \sqrt{\frac{\mu + \hat{\gamma}}{2}} x. \quad (10)$$

For $\alpha \sim \beta \sim \epsilon \ll 1$, where ϵ is an auxiliary small parameter, we expand the solution of Eq. (6) around Eq. (9) as follows:

$$U(x, y, t) = U_0(\chi) + \epsilon U_1(\chi) + \epsilon^2 U_2(\chi) + \dots, \quad (11a)$$

$$V(x, y, t) = V_0(\chi) + \epsilon V_1(\chi) + \epsilon^2 V_2(\chi) + \dots, \quad (11b)$$

where $\chi = x - \Lambda(Y, T_1, T_2, \dots)$ is the longitudinal spatial coordinate in a frame centered at the front position, $x = \Lambda(Y, T_1, T_2, \dots)$, $Y = \sqrt{\epsilon} y$ is the transverse spatial coordinate scaled to describe weak dependence, and $T_i = \epsilon^i t$ ($i = 1, 2, \dots$) are slow time coordinates. In terms of these coordinates partial derivatives in Eq. (6) take the forms

$$\partial_y = \sqrt{\epsilon} \partial_Y, \quad \partial_t = \epsilon \partial_{T_1} + \epsilon^2 \partial_{T_2} + \dots. \quad (12)$$

Inserting Eqs. (11) into Eq. (6) and considering small transverse perturbations, $\Lambda \sim \epsilon$, we obtain at order ϵ

$$\mathcal{M} \begin{pmatrix} U_1 \\ V_1 \end{pmatrix} = \begin{pmatrix} f_1 \\ f_2 \end{pmatrix}, \quad (13)$$

where $f_{1,2} = f_{1,2}(U_0, V_0, \partial_\chi; \alpha, \beta)$ are odd functions of χ and \mathcal{M} is the linear operator

$$\mathcal{M} = \begin{bmatrix} \mathcal{H}_1 & 2U_0 V_0 + \nu \\ 2U_0 V_0 - \nu & \mathcal{H}_2 \end{bmatrix},$$

with

$$\mathcal{H}_1 = -(\mu + \gamma) - \partial_x^2 + 3U_0^2 + V_0^2, \quad \mathcal{H}_2 = -(\mu - \gamma) - \partial_x^2 + 3V_0^2 + U_0^2.$$

Solvability of Eq. (13) requires the right-hand side of this equation to be orthogonal to the null vector \mathcal{E} of \mathcal{M}^\dagger , the adjoint of \mathcal{M} . We evaluated \mathcal{E} numerically and found it to be an even function of χ . Since f_1 and f_2 are odd functions of χ the solvability condition is automatically satisfied. For the same reason U_1 and V_1 must be odd too (i.e. they preserve the symmetry of the zero-order approximation, U_0, V_0).

Proceeding to order ϵ^2 we find

$$\mathcal{M} \begin{pmatrix} U_2 \\ V_2 \end{pmatrix} = \begin{bmatrix} (\partial_{T_1} \Lambda - \partial_Y^2 \Lambda) U_0' + g_1 \\ (\partial_{T_1} \Lambda - \partial_Y^2 \Lambda) V_0' + g_2 \end{bmatrix}, \quad (14)$$

where the prime denotes derivation with respect to the argument and

$$g_{1,2} = g_{1,2}(U_0, V_0, U_1, V_1, \partial_\chi; \alpha, \beta)$$

are odd functions of χ . Solvability of Eq. (14) leads to

$$\partial_{T_1} \Lambda = \partial_Y^2 \Lambda. \quad (15)$$

Using Eq. (15) into Eq. (14) we conclude that U_2 and V_2 are again odd functions of χ (i.e. preserve the symmetry of the lower order approximations).

Proceeding to order ϵ^3 we find

$$\mathcal{M} \begin{pmatrix} U_3 \\ V_3 \end{pmatrix} = \begin{bmatrix} \partial_{T_2} \Lambda U_0' + \alpha(\partial_Y^2 \Lambda) V_0' + (\partial_Y \Lambda)^2 U_0'' + h_1 \\ \partial_{T_2} \Lambda V_0' - \alpha(\partial_Y^2 \Lambda) U_0' + (\partial_Y \Lambda)^2 V_0'' + h_2 \end{bmatrix}, \quad (16)$$

where

$$h_{1,2} = h_{1,2}(U_0, V_0, U_1, V_1, U_2, V_2, \partial_\chi; \alpha, \beta)$$

are odd functions of χ . Solvability of Eq. (16), yields

$$\partial_{T_2} \Lambda = -\alpha \Sigma \partial_Y^2 \Lambda, \quad (17)$$

where

$$\Sigma = \frac{\int_{-\infty}^{\infty} (\mathcal{E}_1 V_0' - \mathcal{E}_2 U_0') d\chi}{\int_{-\infty}^{\infty} (\mathcal{E}_1 U_0' + \mathcal{E}_2 V_0') d\chi}, \quad (18)$$

and \mathcal{E}_1 and \mathcal{E}_2 are the components of the null vector \mathcal{E} . Inserting Eqs. (15) and (17) into Eq. (12), we obtain

$$\partial_t \Lambda = D \partial_y^2 \Lambda, \quad (19)$$

where

$$D = 1 - \alpha \Sigma. \quad (20)$$

The sign of D determines the stability of the Ising front to transverse perturbations; the front is stable (unstable) when $D > 0$ ($D < 0$) and the condition $D = 0$ gives the instability threshold $\gamma = \gamma_T$.

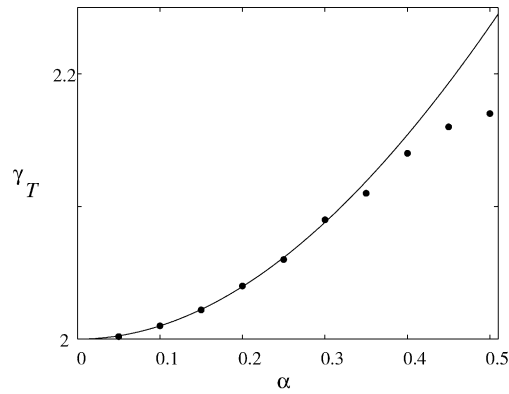


Fig. 6. The transverse instability threshold, γ_T , as a function of α . The solid curve represents the approximation of γ_T given by Eq. (24) and the solid circles denote results of the two-dimensional eigenvalue analysis of the Ising front. Parameters: $\mu = 0.5$, $\nu = 2$, $\beta = 0$.

To evaluate this threshold we need to calculate the integrals in Eq. (18) which we first do numerically. The calculation yields the solid circles in Fig. 4, which are in good agreement with the results of a numerical two-dimensional eigenvalue analysis of the Ising front marked in Fig. 4 by crosses.

An approximate analytical expression for γ_T can be obtained if we restrict ourselves to the high edge regime of the 2:1 tongue boundary [12], $\hat{\gamma}/\gamma \ll 1$, and to the vicinity of the Hopf bifurcation, $\mu/\gamma \ll 1$. Under these conditions

$$\mathcal{M}^\dagger \approx \begin{bmatrix} \mathcal{H}_1 - \nu & \\ \nu & \mathcal{H}_2 \end{bmatrix}, \tag{21}$$

and

$$\mathcal{E}_1 \approx U'_0, \quad \mathcal{E}_2 \approx -V'_0. \tag{22}$$

Inserting Eq. (22) into Eq. (18) we obtain

$$D \approx 1 - \frac{\alpha\nu}{\sqrt{\gamma^2 - \nu^2}}. \tag{23}$$

The threshold of the transverse instability, $D = 0$, now becomes

$$\gamma_T \approx \nu\sqrt{1 + \alpha^2}. \tag{24}$$

where the product $\nu\alpha$ is assumed to be positive. We found a good agreement between the analytical approximation (24) of γ_T and the two-dimensional eigenvalue analysis of the Ising front for small $\hat{\gamma}/\gamma$ as shown in Fig. 4 and for small α values as presented in Fig. 6.

4. Spatial patterns outside the 2:1 resonance tongue

In the previous section, we related resonant patterns, within the 2:1 resonance tongue, to the existence of Ising fronts. The patterns take the form of large stationary domains, possibly coexisting with stripe patterns, in the range where the Ising front is transversely stable, and appear as labyrinths beyond the transverse front instability. Surprisingly, these resonant labyrinthine patterns persist outside the 2:1 resonance tongue ($\gamma < \gamma_b$) where Ising front

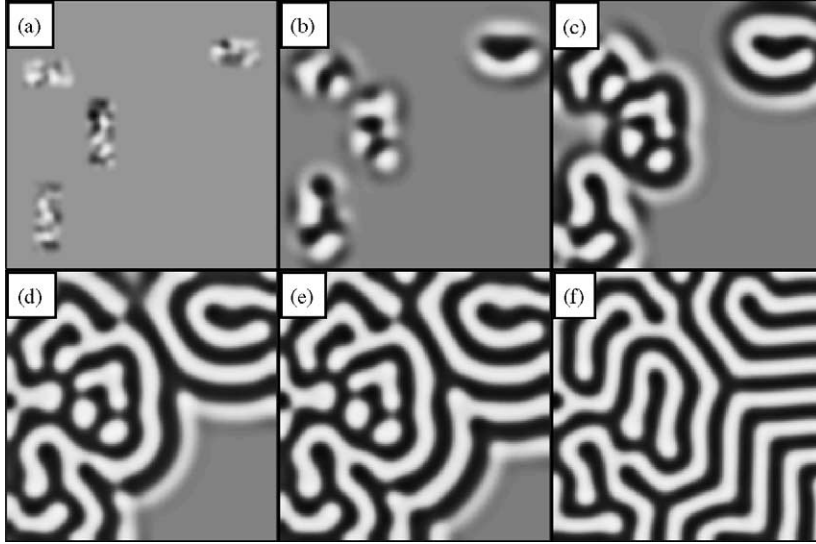


Fig. 7. A numerical solution of Eq. (6) in the range $\gamma < \gamma_b$ (but sufficiently close to γ_b), showing the gradual nucleation of a stationary pattern from uniform oscillations. The uniform oscillations correspond, in the original system, to unlocked oscillations while the asymptotic stationary pattern corresponds to resonant labyrinthine standing waves. Note that the resonant labyrinthine pattern exists in a range where uniform oscillations are not resonant. The frames (a)–(f) show the U field at successive time steps: $t = 0, 4, 8, 13, 18, 1400$. Neumann boundary conditions were used on a $x = [0, 77], y = [0, 77]$ physical grid. Parameters: $\mu = 0.5, \nu = 2.0, \alpha = 0.5, \beta = 0$ and $\gamma = 1.95$.

solutions no longer exist [16,20]. Fig. 7 shows how an asymptotic stationary labyrinthine pattern develops outside the resonance tongue. The asymptotic pattern is very similar to that obtained inside the 2:1 resonance tongue (see Fig. 5). The formation mechanism, however, is different; initial nuclei expand through successive stripe by stripe growth into the surrounding unlocked oscillations.

In this section, we investigate the conditions and mechanisms that give rise to stationary solutions of Eq. (6), or resonant patterns of the original system, outside the 2:1 resonance tongue. We further study their existence range and their stability to secondary instabilities such as zigzag. We find two different realizations of stationary patterns outside the 2:1 tongue: (i) the stationary patterns coexist with stable unlocked uniform oscillations, (ii) the stationary patterns are the only attractor.

In Ref. [20] we identified a codimension 2 point where the Hopf bifurcation to uniform oscillations coincides with a finite wavenumber instability of the $A = 0$ rest state. In the following we show, using a weakly nonlinear analysis, how the two realizations of resonant standing waves outside the 2:1 tongue relate to the coupling between a Hopf mode ($k_0 = 0, \omega_0 \neq 0$) and a finite wavenumber Turing mode ($k_0 \neq 0, \omega_0 = 0$). We further show that these standing waves are unstable to zigzag perturbations as Fig. 15 indicates. With appropriate initial conditions they may appear indistinguishable from the labyrinthine patterns inside the 2:1 tongue.

We begin with a linear stability analysis of the rest state, $(U, V) = (0, 0)$, to inhomogeneous perturbations of the form

$$\begin{pmatrix} U \\ V \end{pmatrix} = \begin{pmatrix} u_k \\ v_k \end{pmatrix} e^{\sigma t + i k x}. \quad (25)$$

Inserting this form in Eq. (6) we obtain the dispersion relation

$$\sigma(k) = \mu - k^2 + \sqrt{\gamma^2 - (\nu - \alpha k^2)^2}. \quad (26)$$

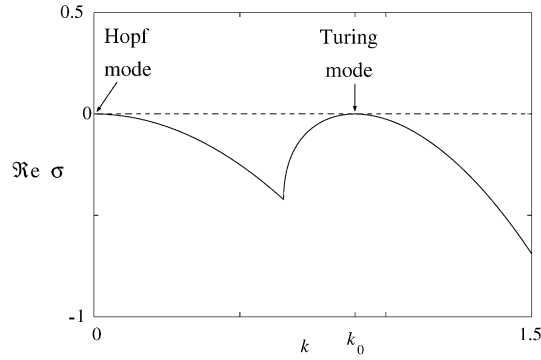


Fig. 8. The growth rate (real part of σ) of perturbations around the $A = 0$ state at the codimension 2 point, $\mu = 0$, $\gamma = \gamma_c$. Two modes become marginal at this point, a Hopf zero- k mode and a Turing finite- k mode. Parameters: $\mu = 0$, $\nu = 2.0$, $\alpha = 0.5$, $\gamma = \gamma_c \approx 1.8$.

At the codimension 2 point, $\mu = 0$, $\gamma = \gamma_c$, where

$$\gamma_c = \frac{\nu}{\sqrt{1 + \alpha^2}}, \quad (27)$$

the Hopf ($k = 0$, $\omega = \omega_0$) and the Turing ($k = k_0$, $\omega = 0$) modes simultaneously become marginal as Fig. 8 shows. The wavenumber k_0 and the frequency ω_0 are given by

$$k_0^2 = \frac{\nu\alpha}{1 + \alpha^2}, \quad (28a)$$

$$\omega_0 = \frac{\nu\alpha}{\sqrt{1 + \alpha^2}}. \quad (28b)$$

Note that if we restrict ourselves to the high frequency edge of the 2:1 tongue ($\nu > 0$) we must choose $\alpha > 0$. Also, if we want the codimension 2 point to lie outside the 2:1 tongue we have to choose $\beta < \alpha$ for at $\beta = \alpha$ the Turing mode becomes marginal at the tongue boundary, i.e. $\gamma_c = \gamma_b$.

4.1. Amplitude equations for the Hopf–Turing bifurcation

In the vicinity of the codimension 2 point, where $d := \gamma - \gamma_c \sim \mu \ll 1$, we can expand solutions of Eq. (6) as

$$\begin{pmatrix} U \\ V \end{pmatrix} = \sqrt{\mu} \begin{pmatrix} U_0 \\ V_0 \end{pmatrix} + \mu \begin{pmatrix} U_1 \\ V_1 \end{pmatrix} + \mu^{3/2} \begin{pmatrix} U_2 \\ V_2 \end{pmatrix} + \dots, \quad (29)$$

where

$$\begin{pmatrix} U_0 \\ V_0 \end{pmatrix} = \mathbf{e}_0 B_0 e^{i\omega_0 t} + \mathbf{e}_k B_k e^{ik_0 x} + \text{c.c.} \quad (30)$$

We assume that $\tilde{d} := d/\mu$ and γ_c are of order unity. The complex amplitudes $B_0(X, Y_1, T)$ and $B_k(X, Y_2, T)$ in Eq. (30) describe weak spatiotemporal modulations of the (relatively) fast oscillations associated with the Hopf mode and of the strong spatial variations associated with the Turing mode. The weak dependence is expressed by the introduction of the slow variables $T = \mu t$, $X = \sqrt{\mu}x$, $Y_1 = \sqrt{\mu}y$ and $Y_2 = \mu^{1/4}y$. The different scales used for the y coordinate stem from the different states (uniform versus stripes) the amplitudes modulate [34–36]. The

eigenvectors \mathbf{e}_0 and \mathbf{e}_k correspond to the eigenvalues $\sigma(0)$ and $\sigma(k_0)$, respectively, and are given by

$$\mathbf{e}_0 = \begin{pmatrix} \frac{1+i\alpha}{\rho} \\ 1 \end{pmatrix}, \quad \mathbf{e}_k = \begin{pmatrix} \eta \\ 1 \end{pmatrix},$$

where $\rho = \sqrt{1+\alpha^2}$ and $\eta = \alpha + \rho$.

Inserting the expansion (29) into Eq. (6) we obtain at order μ

$$\mathcal{M} \begin{pmatrix} U_1 \\ V_1 \end{pmatrix} = -(2\partial_X \partial_x + \partial_{Y_2}^2) \begin{pmatrix} U_0 - \alpha V_0 \\ \alpha U_0 + V_0 \end{pmatrix}, \quad (31)$$

where

$$\mathcal{M} = \begin{bmatrix} -\partial_t + \gamma_c + \partial_x^2 & -\nu - \alpha \partial_x^2 \\ \nu + \alpha \partial_x^2 & -\partial_t - \gamma_c + \partial_x^2 \end{bmatrix}.$$

Defining an inner product as

$$\langle f, g \rangle := \frac{\omega_0 k_0}{(2\pi)^2} \int \int f^* g \, dX \, dT, \quad (32)$$

where the integrals are evaluated over the temporal oscillation period and over the stripe wavelength, the adjoint operator is

$$\mathcal{M}^\dagger = \begin{bmatrix} \partial_t + \gamma_c + \partial_x^2 & \nu + \alpha \partial_x^2 \\ -\nu - \alpha \partial_x^2 & \partial_t - \gamma_c + \partial_x^2 \end{bmatrix}, \quad (33)$$

and its null vector is

$$\Xi = \begin{pmatrix} -\frac{(1+i\alpha)}{\rho} \\ 1 \end{pmatrix} e^{-i\omega_0 t} + \begin{pmatrix} 1 \\ \alpha - \rho \end{pmatrix} e^{-ik_0 x}. \quad (34)$$

The solvability condition associated with Eq. (31) is automatically satisfied and we can proceed to solving this equation. We find

$$\begin{pmatrix} U_1 \\ V_1 \end{pmatrix} = C \begin{pmatrix} U_0 \\ V_0 \end{pmatrix} + \left\{ \begin{pmatrix} 0 \\ \frac{\rho^3}{\nu} \end{pmatrix} \mathcal{D} B_k e^{ik_0 x} + \text{c.c.} \right\}. \quad (35)$$

where $\mathcal{D} = 2ik_0 \partial_X + \partial_{Y_2}^2$ and C is an arbitrary constant which for simplicity, we set to zero.

Proceeding to order $\mu^{3/2}$ we obtain

$$\mathcal{M} \begin{pmatrix} U_2 \\ V_2 \end{pmatrix} = (\mathcal{N}_0 - \mathcal{L}_0) \begin{pmatrix} U_0 \\ V_0 \end{pmatrix} - \mathcal{L}_1 \begin{pmatrix} U_1 \\ V_1 \end{pmatrix}, \quad (36)$$

where

$$\mathcal{L}_0 = \begin{bmatrix} 1 + \tilde{d} + \partial_X^2 - \partial_T & -\alpha \partial_X^2 \\ \alpha \partial_X^2 & 1 - \tilde{d} + \partial_X^2 - \partial_T \end{bmatrix}, \quad \mathcal{N}_0 = (U_0^2 + V_0^2) \begin{bmatrix} 1 & -\beta \\ \beta & 1 \end{bmatrix},$$

$$\mathcal{L}_1 = (2\partial_X \partial_x + \partial_{Y_2}^2) \begin{bmatrix} 1 & -\alpha \\ \alpha & 1 \end{bmatrix}.$$

Solvability of Eq. (36) yields two coupled equations for the amplitudes B_0 and B_k :

$$\partial_T B_0 = \left(1 - \frac{i}{\alpha} \tilde{d}\right) B_0 - (4 + im_1) |B_0|^2 B_0 - (8\rho\eta + im_2) |B_k|^2 B_0 + (1 + i\rho)(\partial_X^2 + \partial_{Y_1}^2) B_0, \quad (37a)$$

$$\partial_T B_k = \left(1 + \frac{\rho}{\alpha} \tilde{d}\right) B_k - 6\rho\eta \left(1 - \frac{\beta}{\alpha}\right) |B_k|^2 B_k - 4 \left(2 - 3\frac{\beta}{\alpha}\right) |B_0|^2 B_k - \frac{\rho^2}{2k_0^2} (2ik_0 \partial_x + \partial_{Y_2}^2)^2 B_k, \quad (37b)$$

where

$$m_1 = \frac{2(2\rho^2 + 1)\beta}{\alpha\rho}, \quad m_2 = \frac{4[2\alpha\rho(\alpha + 1) + (3\rho + \alpha)]\beta}{\alpha} - 4\eta.$$

Finally, by rescaling Eqs. (37) back to the relatively fast space–time scales we obtain the following approximation to Eq. (6) in the vicinity of the codimension 2 point:

$$\begin{pmatrix} U \\ V \end{pmatrix} = \mathbf{e}_0 A_0 e^{i\omega_0 t} + \mathbf{e}_k A_k e^{ik_0 x} + \text{c.c.} + \dots \quad (38)$$

where the ellipses denote high order corrections and the amplitudes A_0 and A_k satisfy

$$\partial_t A_0 = \left(\mu - \frac{i}{\alpha} d\right) A_0 - (4 + im_1) |A_0|^2 A_0 - (8\rho\eta + im_2) |A_k|^2 A_0 + (1 + i\rho) \nabla^2 A_0, \quad (39a)$$

$$\partial_t A_k = \left(\mu + \frac{\rho}{\alpha} d\right) A_k - 6\rho\eta \left(1 - \frac{\beta}{\alpha}\right) |A_k|^2 A_k - 4 \left(2 - 3\frac{\beta}{\alpha}\right) |A_0|^2 A_k - \frac{\rho^2}{2k_0^2} (2ik_0 \partial_x + \partial_y^2)^2 A_k. \quad (39b)$$

4.2. Hopf and Turing pure-mode solutions

Eqs. (39) admit two families of pure-mode solutions and a mixed-mode solution [37,38]. The pure-mode solutions are

$$\tilde{A}_0 = \frac{1}{2} \sqrt{\mu - K^2} e^{i(Kx - \vartheta t) + i\psi_0}, \quad \tilde{A}_k = 0; \quad (40a)$$

and

$$\tilde{A}_0 = 0, \quad \tilde{A}_k = \sqrt{\frac{\alpha\mu + d\rho - 2\alpha\rho^2 K^2}{6\rho\eta(\alpha - \beta)}} e^{iKx + i\psi_k}. \quad (40b)$$

The phases ψ_0 and ψ_k are arbitrary constants which we set to zero and $\vartheta = d/\alpha + \mu m_1/4$. In the context of the original system, the uniform-oscillation solution (40a) corresponds to unlocked uniform oscillations, while the stationary uniform solution (40b) represents resonant standing waves.

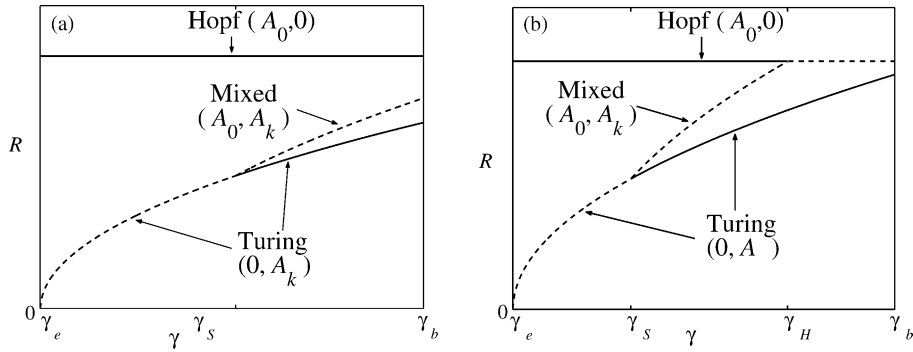


Fig. 9. Bifurcation diagrams for uniform solutions of Eq. (39) showing the existence and stability ranges of the two pure mode solutions and the mixed mode solution in a forcing range extending to the tongue boundary $\gamma = \gamma_b$. The vertical axis is $R = \sqrt{R_0^2 + R_k^2}$. The solid (dashed) curves denote stable (unstable) solutions. (a) $\beta < \beta_B$ and the oscillatory solution $(\tilde{A}_0, 0)$ is stable up to the tongue boundary. (b) $\beta > \beta_B$ and the oscillatory solution loses stability at $\gamma = \gamma_H < \gamma_b$. Parameters: $\mu = 0.5, \nu = 2, \alpha = 0.5$, (a) $\beta = 0$, and (b) $\beta = 0.1$.

We first study the linear stability of the uniform ($K = 0$) solutions (40a) and (40b) by reducing the system (39) to equations for the absolute values of the amplitudes A_0 and A_k [39]:

$$\dot{R}_0 = \mu R_0 - 4R_0^3 - 8\rho\eta R_k^2 R_0, \quad \dot{R}_k = \left(\mu + \frac{d}{\alpha}\right) R_k - 6\rho\eta \left(1 - \frac{\beta}{\alpha}\right) R_k^3 - 4 \left(2 - \frac{3\beta}{\alpha}\right) R_0^2 R_k, \quad (41)$$

where $R_0 := |A_0|$ and $R_k := |A_k|$. Fig. 9 shows bifurcation diagrams for the uniform oscillatory and stationary solutions (40a) and (40b) as obtained by analyzing Eqs. (41). The stationary solution (40b) exists above γ_e where

$$\gamma_e = \gamma_c - \frac{\mu\alpha}{\sqrt{1+\alpha^2}} = \frac{\nu - \mu\alpha}{\sqrt{1+\alpha^2}}, \quad (42)$$

and becomes stable at $\gamma = \gamma_S$ where

$$\gamma_S = \gamma_c - \frac{\mu(\alpha + 3\beta)}{4\sqrt{1+\alpha^2}} = \frac{\nu - \mu(\alpha + 3\beta)/4}{\sqrt{1+\alpha^2}}. \quad (43)$$

The oscillatory solution (40a) exists for all $\gamma < \gamma_b$ (provided $\mu > 0$) but the stability of this solution depends on the value of β . For $\beta < \beta_B$, where β_B is defined below, the oscillatory solution is stable up to the tongue boundary $\gamma = \gamma_b$. For $\beta > \beta_B$ the stability range of (40a) reduces to $\gamma < \gamma_H$ where γ_H is smaller than γ_b and is given by

$$\gamma_H = \gamma_c + \frac{\mu(\alpha - 3\beta)}{\sqrt{1+\alpha^2}} = \frac{\nu + \mu(\alpha - 3\beta)}{\sqrt{1+\alpha^2}}. \quad (44)$$

The value of β_B is determined by the condition $\gamma_H = \gamma_b$ which leads to the following quartic equation for β_B :

$$[\nu + \mu(\alpha - 3\beta_B)]\sqrt{1 + \beta_B^2} - [\nu - \mu\beta_B]\sqrt{1 + \alpha^2} = 0. \quad (45)$$

The mixed mode solution and its stability properties will be studied elsewhere [40]. We only note here that this solution is unstable as long as $\gamma_H > \gamma_S$ which is realized for $\beta < \beta_M$ where

$$\beta_M = \frac{5}{9}\alpha. \quad (46)$$

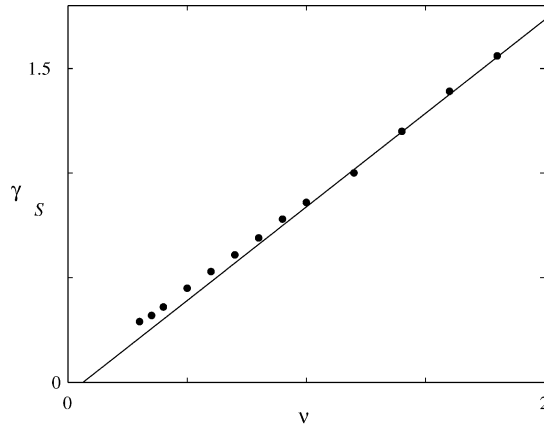


Fig. 10. The stability threshold γ_S for resonant standing-wave solutions. The solid line describes Eq. (43) while the solid circles represent results of numerical solutions of Eq. (6). The parameter values are the same as in Fig. 4.

Using these results we can distinguish among three stability ranges for $\beta_B < \beta < \beta_M$:

- (i) $\gamma < \gamma_S$, where only the oscillatory solution (40a) is stable;
- (ii) $\gamma_H < \gamma < \gamma_b$, where only the stationary solution (40b) is stable;
- (iii) $\gamma_S < \gamma < \gamma_H$, where both solutions (40) are stable.

When $\beta < \beta_B$ the range (ii) disappears and the bistability range (iii) extends to the tongue boundary $\gamma = \gamma_b$.

To test the amplitude Eq. (39) we compared the prediction of Eq. (43) for γ_S (the instability threshold for stationary stripes) with numerical solutions of Eq. (6). Fig. 10 indicates a good agreement for ν values of order unity. A deviation develops at small ν values, but when $\nu \sim \mu$, B_k varies on the scale k_0^{-1} and the analysis is no longer valid.

4.3. Hopf–Turing competition

Using the stability results described above we can distinguish between two different realizations of resonant standing waves (of the original system) outside the 2:1 tongue boundary. When $\beta > \beta_B$ there is a range just below the tongue boundary, $\gamma_H < \gamma < \gamma_b$, where unlocked uniform oscillations are unstable and resonant standing waves are the only stable state. In this case, resonant behavior develops no matter what the initial conditions are. When $\beta < \beta_B$ resonant standing waves and unlocked oscillations coexist as stable states in a range, $\gamma_S < \gamma < \gamma_b$, extending up to the tongue boundary. In this case the realization of resonant behavior depends on initial conditions.

To gain some insight about the initial conditions that lead to resonant behavior in the case $\beta < \beta_B$ we consider front solutions of Eqs. (39) which are bi-asymptotic to the two coexisting states $(\tilde{A}_0, 0)$ and $(0, \tilde{A}_k)$. The direction of the front propagation determines which of the two states invades into the other and prevails at long times. We therefore look for the threshold value, $\gamma = \gamma_N$, at which the Hopf–Turing front has a zero velocity. An analytical expression for the Hopf–Turing front velocity has been found in Ref. [41]. Using this result we find

$$\gamma_N = \gamma_c + \frac{\mu\alpha(\sqrt{3/2} - 1)}{\sqrt{1 + \alpha^2}} = \frac{\nu + \mu\alpha(\sqrt{3/2} - 1)}{\sqrt{1 + \alpha^2}}. \tag{47}$$

Fig. 11 shows the line γ_N in the ν – γ plane, as obtained from Eq. (47) and the good agreement of this result with numerical solutions of Eq. (39). For $\gamma > \gamma_N$ the $(0, \tilde{A}_k)$ state invades the $(\tilde{A}_0, 0)$ state as Fig. 12 demonstrates. This dominance of the $(0, \tilde{A}_k)$ state implies that any initial state involving at least one island of resonant standing waves

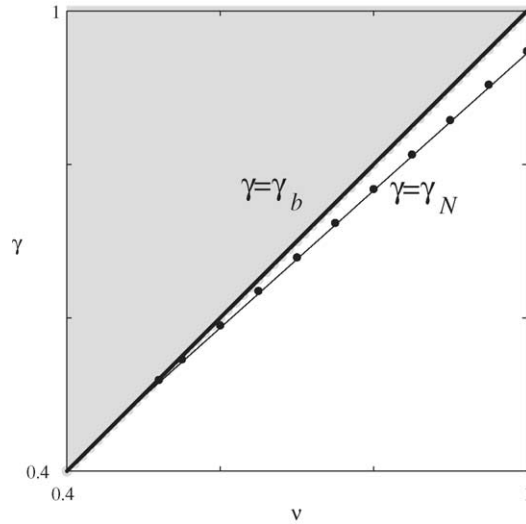


Fig. 11. Dominance range of resonant standing waves outside the 2:1 resonance tongue for $\beta < \beta_B$. For $\gamma_N < \gamma < \gamma_b$ standing waves, $(0, \tilde{A}_k)$, invade unlocked oscillations, $(\tilde{A}_0, 0)$, and become the asymptotic pattern (see Fig. 12). The solid line $\gamma = \gamma_N$ describes Eq. (47) while the solid circles represent results of numerical solutions of Eq. (39). Parameter values are the same as in Fig. 4.

is likely to evolve into a resonant standing-wave pattern occupying the whole system. For $\gamma < \gamma_N$, the $(\tilde{A}_0, 0)$ state is the dominant one and the asymptotic state is unlocked oscillations.

Returning to Fig. 7 which shows the development of standing-wave patterns outside the 2:1 tongue we can now interpret the stripe by stripe growth mechanism as an invasion of the $(0, \tilde{A}_k)$ state (standing waves) into the $(\tilde{A}_0, 0)$ (unlocked oscillations). Fig. 7 applies to the case $\beta < \beta_B$ where the two states stably coexist and to $\gamma > \gamma_N$. When $\beta > \beta_B$ similar stripe by stripe growth can be realized, but unlike the former case, standing waves develop from any initial condition even in the absence of an initial $(0, \tilde{A}_k)$ island that serves as a nucleation center. The growth

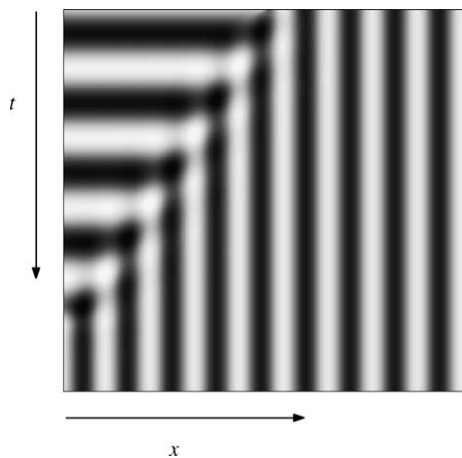


Fig. 12. Invasion of resonant standing waves into unlocked oscillations, obtained by numerical integration of Eq. (39) in the range $\gamma_N < \gamma < \gamma_b$. The solution represents the real part of (U_0, V_0) reconstructed according to Eq. (30). Neumann boundary conditions were used. This behavior reproduces the results of Fig. 7 obtained by solving Eq. (6) with the same parameter values.

mechanism of standing-wave patterns outside the 2:1 tongue is very different from the fingering and tip splitting mechanism that applies inside the tongue [see Fig. 5]. The asymptotic patterns, however, may look very similar as a comparison of Figs. 5 and 7 suggests. This is partly because the standing-wave stripes are unstable to zigzag perturbations as we now show.

4.4. Zigzag instability of the pure Turing mode

Consider the stationary periodic stripe solution given by Eq. (40b). To study the stability of this solution to zigzag perturbations [36], we write

$$\begin{pmatrix} A_0 \\ A_k \end{pmatrix} = \begin{pmatrix} 0 \\ \tilde{A}_k \end{pmatrix} + \begin{pmatrix} \delta A_0 \\ \delta A_k \end{pmatrix}, \quad (48)$$

where

$$\begin{pmatrix} \delta A_0 \\ \delta A_k \end{pmatrix} = \begin{bmatrix} a_{0+}(t) \\ a_{k+}(t) \end{bmatrix} e^{i(Kx+Qy)} + \begin{bmatrix} a_{0-}^*(t) \\ a_{k-}^*(t) \end{bmatrix} e^{i(Kx-Qy)}.$$

Inserting Eq. (48) into Eq. (39), and linearizing around $(0, \tilde{A}_k)$ we obtain two sets of ordinary differential equations

$$\dot{a}_{0\pm} = [\mu - WP - Q^2 - iM]a_{0\pm}, \quad \dot{a}_{k\pm} = - \left[P + \frac{\rho^2}{2k_0^2}(4k_0KQ^2 + Q^4) \right] a_{k\pm} - Pa_{k\mp}, \quad (49)$$

where $P = \mu + \rho d/\alpha - 2\rho^2 K^2$, $W = 4\alpha/[3(\alpha - \beta)]$ and $M = d/\alpha + m_2|\tilde{A}_k|^2 + \rho(K^2 + Q^2)$. Seeking solutions of Eq. (49) in the form

$$a_{0\pm} = \tilde{a}_{0\pm} e^{\lambda_0 t}, \quad (50a)$$

$$a_{k\pm} = \tilde{a}_{k\pm} e^{\lambda_k t}, \quad (50b)$$

we find the following expressions for the perturbation growth rates:

$$\text{Re } \lambda_0^\pm = \mu - WP - Q^2, \quad (51a)$$

$$\lambda_k^\pm = - \frac{\rho^2}{2k_0^2}(4k_0KQ^2 + Q^4) - P \pm P. \quad (51b)$$

The first mode to grow is the Turing phase mode whose growth rate is given by $\lambda_k^+(Q)$. The long-wavelength zigzag instability sets in at $K = 0$ and exists anywhere in the parameter ranges we consider (for which $\mu > 0$ and $\nu\alpha > 0$). Fig. 13 shows the dispersion relation $\lambda_k^+(Q)$ at the onset $K = 0$ and beyond the instability $K < 0$. The maximal growth rate beyond the instability occurs at $Q = Q_0$ where

$$Q_0^2 = -2k_0K. \quad (52)$$

Fig. 14 summarizes the results of the linear stability analysis of stationary stripe solutions (standing waves in the original system) in the γ - K parameter space. The periodic stripe solutions (40b) form at the parabolic dashed curve given by

$$\tilde{\gamma}_e = \gamma_e + 2\alpha\rho K^2. \quad (53)$$

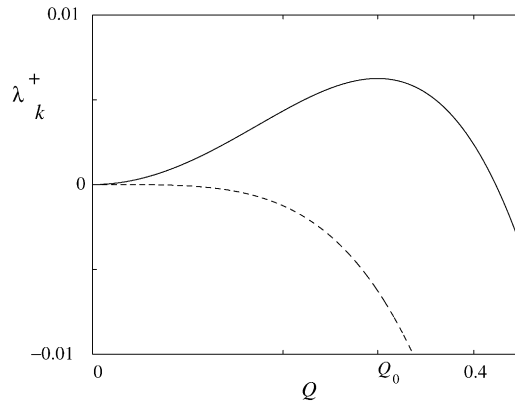


Fig. 13. Growth curves for the zigzag instability of the stationary-stripe solution Eq. (40b). Shown are the growth rates λ_k^+ , as computed from Eq. (51b), at the instability threshold $K = 0$ (dashed curve) and beyond the instability $K = -0.05$ (solid curve). Other parameters: $\nu = 2.0$, $\alpha = 0.5$.

Below the solid parabolic curve, $\gamma = \tilde{\gamma}_S$, where

$$\tilde{\gamma}_S = \gamma_S + 2\alpha\rho K^2. \tag{54}$$

the stripe solutions are unstable to uniform oscillations or traveling waves ($\text{Re } \lambda_0^\pm > 0$). Above this curve stationary stripe patterns become stable but may go through secondary zigzag and Eckhaus instabilities as depicted in the figure. (The Eckhaus instability analysis will be presented elsewhere [27].) Numerical solutions of the forced CGL equation (6) support the above predictions. The stripes are stable for positive K values (that do not cross the Eckhaus instability) while for negative K values (see point “Z” in Fig. 14) the stripes are unstable to zigzag perturbations as Fig. 15 demonstrates. As γ is reduced below $\tilde{\gamma}_S$ (see point “O” in Fig. 14) the stationary stripes lose stability to oscillations, as Fig. 16 demonstrates.

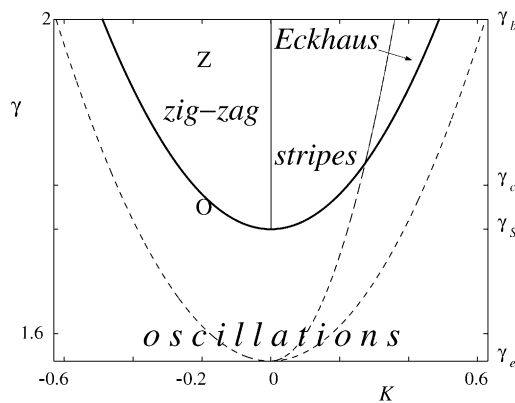


Fig. 14. The neutral stability curve for stationary stripes (thick solid curve) with secondary zigzag and Eckhaus instabilities (thin solid curves). Stationary stripe solutions appear at the dashed parabolic curve but becomes stable only above the solid parabolic curve. In between the two curves uniform oscillations and traveling waves prevail. The points “Z” ($\gamma = 1.95$, $K = -0.2$) and “O” ($\gamma = 1.77$, $K = -0.2$) represent forcing and wavenumber values where the stripe solutions are unstable to zigzag and oscillating patterns, respectively. All the other parameters are the same as in Fig. 7.

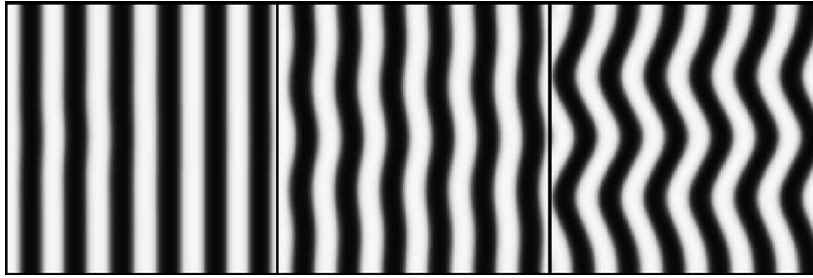


Fig. 15. Numerical solution of the forced CGL equation (6) for negative deviations from k_0 ($K = -0.2$), showing the development of a zig-zag pattern (point “Z” in Fig. 14). The frames (left to right) correspond to $t = 1, 300, 400$. Periodic boundary conditions were used on a $x = y = [0, 51]$ physical grid. Parameters are as in Fig. 14 $\nu = 2, \gamma = 1.95$.

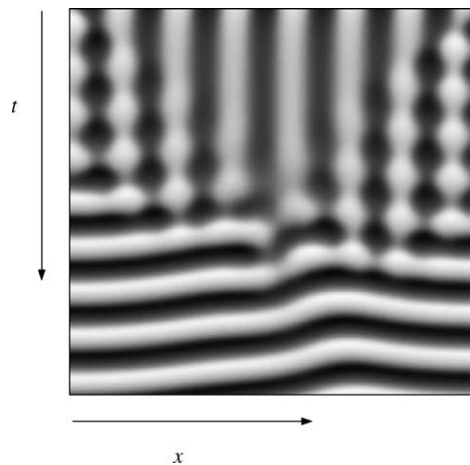


Fig. 16. Numerical solution of the forced CGL equation (6) for negative deviations from k_0 ($K = -0.2$), showing in a space–time plot the development of oscillations (point “O” in Fig. 14). Neumann boundary conditions were used. Parameters are as in Fig. 14, $\nu = 2, \gamma = 1.77$, $x = [0, 64]$ and $t = [0, 60]$.

5. Discussion

We have presented a theoretical study of resonant patterns in oscillatory systems that are subjected to uniform time-periodic forcing at a frequency about twice as large as the unforced system’s frequency. The study is based on the amplitude equation for forced systems undergoing a Hopf bifurcation to uniform oscillations. Resonant patterns are defined in this paper as spatiotemporal patterns where the oscillation frequency at any spatial point is exactly half the forcing frequency.

We find that the range of resonant patterns in the forcing amplitude and frequency ν – γ plane does not coincide with the 2:1 resonance tongue of uniform oscillations. Below the NIB bifurcation, non-resonant traveling waves prevail. Above the NIB bifurcation resonant standing waves prevail, but these extend beyond the tongue of uniform oscillations. For $\beta > \beta_B$ there exists a range, $\gamma_H < \gamma < \gamma_b$, outside the 2:1 tongue where resonant standing waves are the only stable patterns. For $\beta < \beta_B$ resonant standing waves outside the 2:1 tongue coexist with unlocked oscillations. In the range $\gamma_N < \gamma < \gamma_b$, however, the standing-wave patterns are dominant in the sense that nuclei of standing waves grow into unlocked oscillations and become the asymptotic state of the system.

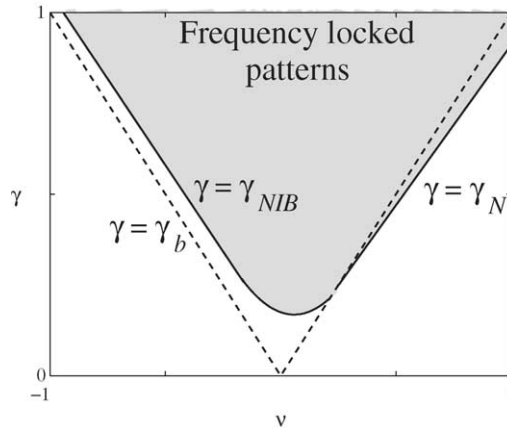


Fig. 17. The 2:1 resonance tongue of uniform oscillations (the dashed boundary) vs. the tongue of resonant patterns (the shaded area with solid boundary). Parameters are as in Fig. 1(b).

Fig. 17 summarizes the regions in the ν - γ plane where resonant patterns prevail along with the 2:1 tongue inside which frequency-locked uniform oscillations exist. The boundary $\gamma = \gamma_{NIB}$, inside the 2:1 tongue, appears to merge with the line $\gamma = \gamma_N$ outside the 2:1 tongue and form together the boundary of the region of resonant patterns. More careful analysis is needed, however, to substantiate this numerical observation.

The resonant standing waves outside the tongue are zigzag unstable and may appear as labyrinthine patterns with appropriate initial conditions [20]. These labyrinths appear indistinguishable from the labyrinths that prevail inside the 2:1 tongue. Their formation mechanism however is quite distinct. While labyrinths inside the tongue develop from a transverse front instability through fingering and tip splitting (see Fig. 5), labyrinths outside the tongue develop through stripe by stripe nucleation from standing-wave nuclei (see Fig. 7). The two mechanisms have been identified recently in experiments on the Belousov–Zhabotinsky reaction [20].

The results described in this paper are restricted to a relatively small volume in the parameter space spanned by μ , ν , α , β , γ . The analysis is based on the forced complex Ginzburg–Landau equation which is valid close to the Hopf bifurcation. We therefore avoided large μ values. The study was originally motivated by experimental observations of resonance labyrinthine patterns on the high right edge of the 2:1 resonant tongue [12]. Accordingly we chose ν to be positive and following Eq. (28), $\alpha > 0$. We also chose α and β to be small (and of the same order of magnitude) to facilitate the analysis of the transverse Ising front instability. We confined ourselves to the case $\beta < 5\alpha/9$ for which resonant standing waves exist outside the 2:1 resonance tongue. The case $\beta > 5\alpha/9$ will be considered elsewhere [40]. Different parameter ranges have been studied in Refs. [16,42] ($\nu < 0$, $\alpha < 0$), and in Ref. [17] ($\alpha \gg \beta \sim \mu$).

Acknowledgments

We thank Anna Lin, Hezi Yizhaq, and Erez Gilad for helpful discussions and comments. This research was supported by the US–Israel Binational Science Foundation, by the Department of Energy under contracts W-7405-ENG-36 and the DOE Office of Science Advanced Computing Research (ASCR) program in Applied Mathematical Sciences. C.E. acknowledges the support of Fondecyt under grant no. 1020374.

References

- [1] V.I. Arnold, *Geometrical Methods in the Theory of Ordinary Differential Equations*, Springer-Verlag, New York, 1983.
- [2] M.H. Jensen, P. Bak, T. Bohr, Transition to chaos by interaction of resonances in dissipative systems. I. Circle maps, *Phys. Rev. A* 30 (1984) 1960–1969.
- [3] L. Glass, J. Sun, Periodic forcing of a limit-cycle oscillator : Fixed points, Arnold tongues, and the global organization of bifurcations, *Phys. Rev. E* 50 (6) (1994) 5077–5084.
- [4] R.C. Hilborn, *Chaos and Nonlinear Dynamics*, Oxford University Press, New York, 1994.
- [5] J.A. Glazier, A. Libchaber, Quasi-periodicity and dynamical systems: an experimentalist's view, *IEEE Trans. Circuits Syst.* 35 (1988) 790–809.
- [6] M. Eiswirth, G. Ertl, Forced oscillations of a self-oscillating surface reaction, *Phys. Rev. Lett.* 60 (15) (1988) 1526–1529.
- [7] P. Couillet, J. Lega, B. Houchmanzadeh, J. Lajzerowicz, Breaking chirality in nonequilibrium systems, *Phys. Rev. Lett.* 65 (1990) 1352–1355.
- [8] P. Couillet, K. Emilsson, Strong resonances of spatially distributed oscillators: a laboratory to study patterns and defects, *Physica D* 61 (1992) 119–131.
- [9] V. Petrov, Q. Ouyang, H.L. Swinney, Resonant pattern formation in a chemical system, *Nature* 388 (1997) 655–657.
- [10] A.L. Lin, A. Hagberg, A. Ardelea, M. Bertram, H.L. Swinney, E. Meron, Four-phase patterns in forced oscillatory systems, *Phys. Rev. E* 62 (2000) 3790–3798.
- [11] H. Chate, A. Pikovsky, O. Rudzick, Forcing oscillatory media: phase kinks vs. synchronization, *Physica D* 131 (1999) 17–30.
- [12] A.L. Lin, M. Bertram, K. Martinez, H.L. Swinney, A. Ardelea, G.F. Carey, Resonant phase patterns in a reaction–diffusion system, *Phys. Rev. Lett.* 84 (2000) 4240–4243.
- [13] V.K. Vanag, L.F. Yang, M. Dolnik, A.M. Zhabotinsky, I.R. Epstein, Oscillatory cluster patterns in a homogeneous chemical system with global feedback, *Nature* 406 (6794) (2000) 389–391.
- [14] V.K. Vanag, A.M. Zhabotinsky, I.R. Epstein, Pattern formation in the Belousov–Zhabotinsky reaction with photochemical global feedback, *J. Phys. Chem. A* 104 (49) (2000) 11566–11577.
- [15] V.K. Vanag, A.M. Zhabotinsky, I.R. Epstein, Oscillatory clusters in the periodically illuminated, spatially extended Belousov–Zhabotinsky reaction, *Phys. Rev. Lett.* 86 (3) (2001) 552–555.
- [16] H.-K. Park, Frequency locking in spatially extended systems, *Phys. Rev. Lett.* 86 (2001) 1130–1133.
- [17] D. Gomila, P. Colet, G.L. Oppo, M.S. Miguel, Stable droplets and growth laws close to the modulational instability of a domain wall, *Phys. Rev. Lett.* 87 (19) (2001) 194101.
- [18] R. Gallego, D. Walgraef, M. San Miguel, R. Toral, Transition from oscillatory to excitable regime in a system forced at three times its natural frequency, *Phys. Rev. E* 64 (5) (2001) 056218.
- [19] J. Kim, J. Lee, B. Kahng, Harmonic forcing of an extended oscillatory system: Homogeneous and periodic solutions, *Phys. Rev. E* 65 (4) (2002) 046208.
- [20] A. Yochelis, A. Hagberg, E. Meron, A.L. Lin, H.L. Swinney, Development of standing-wave labyrinthine patterns, *SIADS* 1 (2) (2002) 236–247 <http://epubs.siam.org/sam-bin/dbq/article/39711>.
- [21] K. Martinez, A.L. Lin, R. Kharrazian, X. Sailer, H.L. Swinney, Resonance in periodically inhibited reaction–diffusion systems, *Physica D* 2 (2002) 168–169.
- [22] E. Meron, Phase fronts and synchronization patterns in forced oscillatory systems, *Discrete Dyn. Nat. Soc.* 4 (3) (2000) 217–230.
- [23] J.M. Gambaudo, Perturbation of a Hopf bifurcation by an external time-periodic forcing, *J. Diff. Eq.* 57 (1985) 172–199.
- [24] C. Elphick, G. Iooss, E. Tirapegui, Normal form reduction for time-periodically driven differential equations, *Phys. Lett. A* 120 (1987) 459–463.
- [25] C. Elphick, A. Hagberg, E. Meron, A phase front instability in periodically forced oscillatory systems, *Phys. Rev. Lett.* 80 (22) (1998) 5007–5010.
- [26] C. Elphick, A. Hagberg, E. Meron, Multiphase patterns in periodically forced oscillatory systems, *Phys. Rev. E* 59 (5) (1999) 5285–5291.
- [27] A. Yochelis, Pattern formation in periodically forced oscillatory systems, Ph.D. Thesis, Ben-Gurion University, 2003.
- [28] A. Hagberg, E. Meron, Pattern formation in non-gradient reaction–diffusion systems: the effects of front bifurcations, *Nonlinearity* 7 (1994) 805–835.
- [29] A. Hagberg, E. Meron, From labyrinthine patterns to spiral turbulence, *Phys. Rev. Lett.* 72 (15) (1994) 2494–2497.
- [30] S. Sarker, S.E. Trullinger, A.R. Bishop, Solitary-wave solution for a complex one-dimensional field, *Phys. Lett. A* 59 (4) (1976) 255–258.
- [31] C. Elphick, A. Hagberg, E. Meron, B. Malomed, On the origin of traveling pulses in bistable systems, *Phys. Lett. A* 230 (1997) 33–37.
- [32] D.V. Skryabin, A. Yulin, D. Michaelis, W.J. Firth, G.L. Oppo, U. Peschel, F. Lederer, Perturbation theory for domain walls in the parametric Ginzburg–Landau equation, *Phys. Rev. E* 64 (5) (2001) 056618.
- [33] C. Elphick, Dynamical approach to the Ising–Bloch transition in $3 + 1$ dimensional time periodically driven dynamical systems, *Physica D*, submitted for publication.
- [34] A.C. Newell, J.A. Whitehead, Finite bandwidth, finite amplitude convection, *J. Fluid Mech.* 38 (1969) 279–303.
- [35] L.A. Segel, Distant side-walls cause slow amplitude modulation of cellular convection, *J. Fluid Mech.* 38 (1969) 203–224.

- [36] M.C. Cross, P.C. Hohenberg, Pattern formation outside of equilibrium, *Rev. Mod. Phys.* 65 (3) (1993) 851–1112.
- [37] J.P. Keener, Secondary bifurcation in nonlinear diffusion-reaction equations, *Stud. Appl. Math.* 55 (3) (1976) 187–211.
- [38] H. Kidachi, On mode interactions in reaction diffusion equation with nearly degenerate bifurcations, *Prog. Theor. Phys.* 63 (4) (1980) 1152–1169.
- [39] J.D. Crawford, Introduction to bifurcation theory, *Rev. Mod. Phys.* 63 (4) (1991) 991–1037.
- [40] A. Yochelis, C. Elphick, A. Hagberg, E. Meron, Frequency locking in extended systems: the impact of a Turing mode, in press.
- [41] M. Or-Guil, M. Bode, Propagation of Turing–Hopf fronts, *Physica A* 249 (1998) 174–178.
- [42] H.-K. Park, M. Bär, Spiral destabilization by resonant forcing, *Europhys. Lett.* 65 (2004) 873–879.